

Theoretical and Experimental Analysis of In Vivo Wheeled Mobility

Mark Rentschler, Jason Dumpert, Adnan Hadzialic,
Stephen R. Platt, Shane Farritor
Department of Mechanical Engineering
University of Nebraska-Lincoln,
Lincoln, NE 68588 U.S.A.
sfarritor@unl.edu

Dmitry Oleynikov
Department of Surgery
University of Nebraska Medical Center
Omaha, NE 68198-3280 U.S.A.

Karl Iagnemma
Department of Mechanical Engineering
Massachusetts Institute of Technology
Cambridge, MA, 02215 U.S.A.

Abstract— Laparoscopy is abdominal surgery performed with long tools inserted through small incisions. The use of small incisions reduces patient trauma, but also eliminates the surgeon's ability to directly view and touch the surgical environment. These limitations generally restrict the application of laparoscopy to less complex procedures. Large robots external to the patient have been used to aid in the manipulation of the tools and improve dexterity. This paper presents a theoretical and experimental analysis of miniature *in vivo* robots. The objective is to develop a wireless mobile imaging robot that can be placed inside the abdominal cavity during surgery. Such robots will for the first time allow the surgeon to view the surgical environment from multi-angles. The motion of these *in vivo* robots will not be constrained by the insertion incisions.

Keywords—Surgical Robots; wheeled mobility

I. INTRODUCTION

Minimally invasive surgery is not minor surgery, it is major surgery performed through small incisions [1]. It is surgery performed from a distance. These small incisions are the advantage—reduced patient trauma—and limitation of minimally invasive surgery. These small holes do not allow the surgeon to directly view or touch the surgical environment, and they constrain the motion of the endpoint of the tools and cameras to arcs of a sphere whose center is the insertion point. Vision limitations are significant [2-3] because the current field of view cannot encompass the frequent changes of instruments as they pass through the abdominal cavity. This has led to accidental injury to organs and vascular structures [4-5]. Additional viewpoints—showing the entire body cavity—would be very helpful [1]. Such limitations have slowed the expanded use of laparoscopic techniques. Within about a decade of the first laparoscopic cholecystectomy, 85% of all gall bladder excisions were performed laparoscopically [6]. The overwhelming success of this procedure resulted in high expectations for the rapid, wholesale conversion of many other conventional open procedures to less invasive approaches. The reality is that laparoscopic surgery has not realized this potential. In 2000, less than 3% of colon resections [7] and

only 17% of cardiothoracic surgeries [6] were performed laparoscopically.

Robots have been used to increase the surgeon's dexterity. Several systems exist to help the surgeon precisely manipulate laparoscopic tools. Such systems generally consist of a multi-arm robot that is external to the patient. Each arm manipulates a tool (or camera) that is tele-operated by a surgeon. The robots can filter the natural tremor present in the human hand, correct for the effects of motion reversal, or perform motion scaling to provide greater control of instrument movements in the surgical field. Such systems are generally expensive and have a limited range of motion that is still constrained by the insertion points.

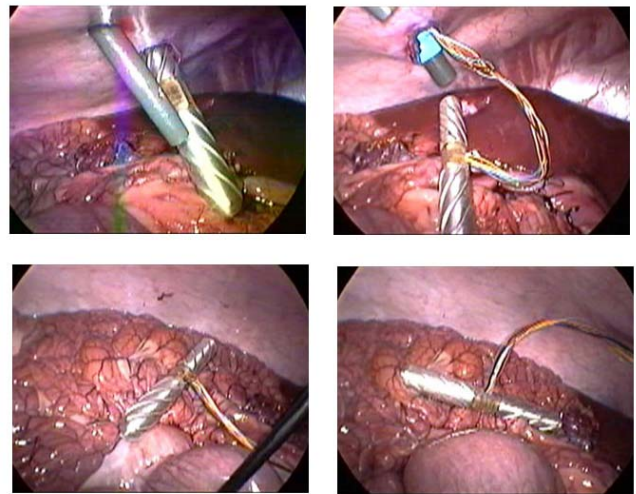


Figure 1. Robot prototype tested during porcine surgery.

This work proposes a new approach to laparoscopy—inserting miniature robotic assistants into the patient. Robotic assistants placed inside the abdominal cavity during surgery have the potential to enhance the capabilities of the surgeon, reduce costs, and improve patient care.

Fig. 1 shows an initial prototype being tested in a porcine (pig) surgery. This paper presents a theoretical analysis of the mobility of this robot on organs. Simulation and experimental results are presented.

II. LITERATURE REVIEW

A. Robot-Assisted Laparoscopy

The use of robotics is currently recognized as the major driving force for the future technological advance of minimally invasive surgery [8-10]. The first application of robotics to direct surgical manipulation in laparoscopic surgery was the Automated Endoscopic System for Optimal Positioning (AESOP) which allows the surgeon to position and stabilize a laparoscopic camera using voice control [11]. This was the first robotic device to receive approval from the Food and Drug Administration (FDA) for clinical use in abdominal surgery [9], and it successfully launched the era of robot-assisted surgery [8]. The ZEUS Robotic Surgical System (Computer Motion) and the da Vinci Surgical System (Intuitive Surgical) are commercially available telerobotic devices that have the potential to permit solo surgery from a remote site. These robots serve in a master-slave relationship with the surgeon, and use separate arms to hold a camera and the surgical instruments. Computerized control systems are used to filter the natural tremor present in the human hand, correct for the effects of motion reversal, and perform motion scaling to provide greater control of instrument movements in the surgical field. These two systems have been available for only a few years, and their efficacy and value are currently being evaluated in randomized clinical trials [8]. A prototype of a third robotic surgical system, ARTEMIS, has been developed in Europe [10]. Tests using animals have shown this to be a highly dexterous system with potentially superior manipulation capabilities compared to the ZEUS and da Vinci systems [8].

Other research has focused on tool designs and end-effectors that restore some of the lost dexterity by including a wrist-like joint [12].

All the above systems of laparoscopic tools and surgical robots are implemented from outside the body and therefore are still fundamentally constrained by the limited access to the abdominal cavity provided by small access ports. Moreover, each of the robotic arms is necessarily long and bulky to accommodate the range of motion required to maneuver the long instruments attached to each arm. Large excursion arcs of the arms lead to collisions outside the patient, and improper placement of the access ports leads to collisions inside the patient [9]. Each arm requires a separate access port into the abdominal cavity, hence the number of incisions is not reduced compared to conventional laparoscopy. These incisions are made as part of the set-up procedure for the robot, so the problems associated with injuries caused by access port insertion remain unaddressed. Similarly, a limited range of motion for the robotic camera can still result in obstructed or incomplete visual feedback. Tool changes still require the removal of the existing tool and the reinsertion of the new one, adding to the overall surgical time and adversely affecting the efficiency of the operation [12-13].

Initial work has begun to address in vivo robotic manipulators and visual feedback [14]. These initial prototypes have demonstrated the potential for future success.

B. Wheeled Mobility

A wheeled mobile robot moving inside an abdominal cavity can be viewed in the general context of wheel-surface interaction. Wheel-terrain interaction has been studied extensively for passenger vehicle applications. First attempts to develop a comprehensive theory applicable to all soils were made at the Land Locomotion Laboratory [15]. Later, these equations were modified because of some inaccuracies during extreme loading conditions. In 1967, Onafeko and Reece developed a better theory for including shear stress with slip during wheel-soil interaction [16]. Wong and Reece (1967) showed that there are both radial and tangential stresses on the wheel-soil interface [17]. It was also shown that these do not only depend on soil properties and wheel dimensions, but slip as well. Special attention was given to performance of wheels in sand. Iagnemma et al. developed an on-line estimation method that identifies key terrain parameters, such as terrain cohesion and internal friction angle, using a simplified form of the classical terramechanics equations [18]. These parameters were then used for traversability prediction.

However, the environment inside the abdomen is much different than any of the studies mentioned above. The wheel interacts with organs that are highly deformable and very slick, and the constitutive relations describing wheel-organ interaction generally do not resemble those of soils. The surface deformation under the weight of the robot in Fig. 1 is very high, sometimes larger than even the wheel diameter. This paper builds on some of the above techniques to simulate wheel-surface interaction of a rigid wheel on a highly deformable, highly elastic, and slick surface.

III. AN *IN VIVO* WHEELED MOBILE ROBOT

The robot being analyzed in this paper is shown in Fig. 2. It is a cylinder that is 15 mm in diameter and 85 mm long. It has two wheels that are independently driven, and a small tail (not shown) to prevent the body from spinning. It has a center space that is sized to hold a small camera. The robot has been tethered in these early tests.

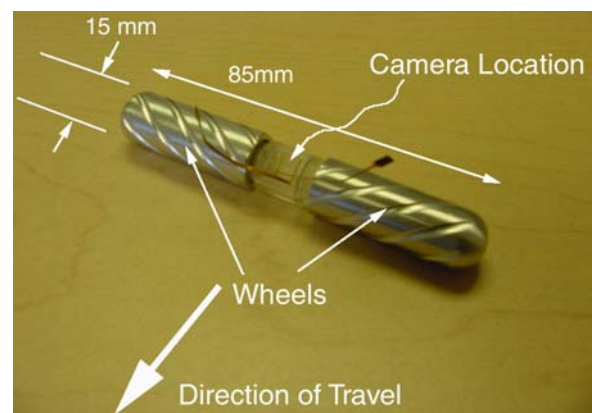
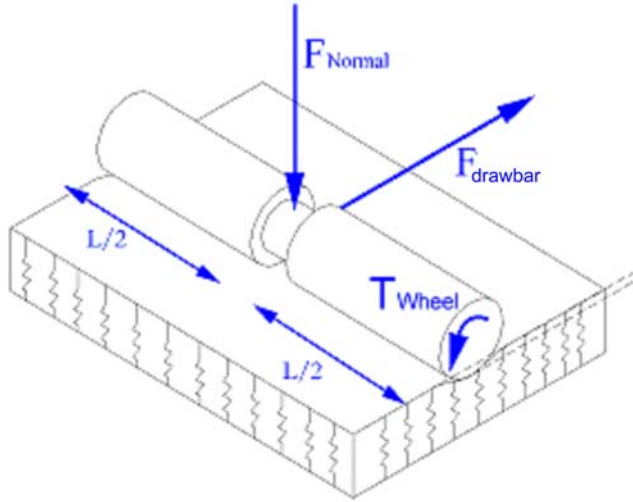


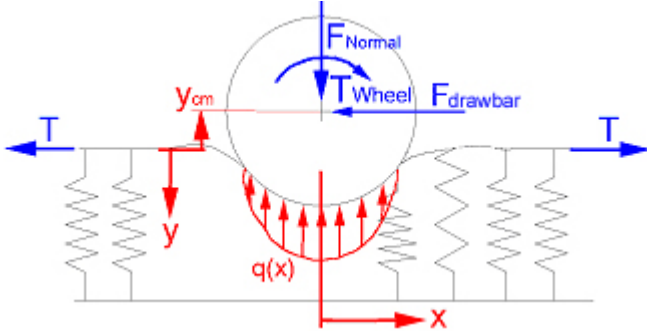
Figure 2. Robot prototype.

IV. WHEEL / TISSUE INTERACTION

The abdominal cavity is a difficult navigational environment for a small robot because human organs are highly deformable and have highly variable surface properties. Any successful mobile robot must be able to traverse these organs without causing damage. The surface mobility of robots has been analyzed using the surface interaction model of Filonenko-Borodich for a membrane on an elastic foundation [19]. As depicted in Fig. 3, the mobility of a wheeled robot can be characterized by the drawbar force (F_{drawbar}) produced. This force is a strong function of the normal force (F_{normal}) between the wheel and the surface, the effective coefficient of friction between the wheel and the surface, and wheel torque (T_{wheel}) [20].



a) Three-dimensional robot model.



b) Two-dimensional model.

Figure 3. Robot model.

A. Mathematical Model

The Filonenko-Borodich model represents the load distribution for an elastic material covered by a membrane with a tension T . The pressure distribution per unit wheel length, $q(x)$, resulting from an object on the membrane is related to the deflection of the surface, $w(x)$, by (1)

$$q(x) = kw(x) - T \frac{d^2w(x)}{dx^2}, \quad (1)$$

where k , is a stiffness for the elastic medium. Stiffness is usually expressed as a ratio of force per unit displacement, but here the stiffness is expressed as surface pressure over the displacement, or the force applied over a given surface area per vertical displacement. The experiments presented in this paper show that the tissue deformation directly forward and behind the wheel is very small compared to the contact length ($\approx 2r \sin^{-1}\left(\frac{a}{r}\right)$) between the surface and the object, Fig. 4.

This implies that the tension in the surface membrane is small and the energy stored in the elastic medium in the areas directly forward and behind the wheel can be neglected.

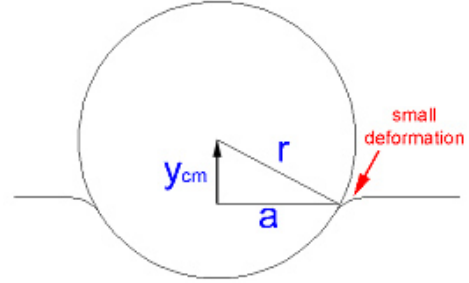


Figure 4. Surface deflection geometry.

Therefore, the reaction force from the elastic material is given by the integration of the pressure distribution over the length of contact ($2a$) in the x direction.

$$F_{\text{reaction}} = \int_{-a}^a L \cdot q(x) dx. \quad (2)$$

For a rigid circular wheel the deflection of the membrane will also be circular and is given by

$$w(x) = y_{\text{wheel}} + y_{\text{cm}} = \sqrt{r^2 - x^2} + y_{\text{cm}}, \quad (3)$$

where y_{cm} is the location of the center of mass of the wheel (a negative number in Fig. 4), y_{wheel} is the circular geometry of the wheel, and r is the radius.

The reaction force can now be found by substituting (3) and (1) into (2) and integrating over the contact area,

$$F_{\text{reaction}} = k \cdot L \cdot \left[a\sqrt{r^2 - a^2} + r^2 \sin^{-1}\left(\frac{a}{r}\right) + 2ay_{\text{cm}} \right]. \quad (4)$$

The relationship between y_{cm} and a (Fig. 4) is given by

$$y_{\text{cm}} = -\sqrt{r^2 - a^2} \quad (6)$$

for situations where $y_{\text{cm}} < 0$. If $y_{\text{cm}} \geq 0$, it is assumed that $a = r$. This relationship is valid if the tension, T , is low.

The vertical (y_{cm}) dynamic response of the system was found by solving the equation of motion shown in (9)

$$m\ddot{y}_{cm} + F_{reaction} = F_{normal}, \quad (9)$$

where F_{normal} equals mass of the robot multiplied by gravity (mg). Using the results from (4), (9) becomes

$$\ddot{y}_{cm} = g - \frac{Lk}{m} r^2 \sin^{-1}\left(\frac{a}{r}\right) - \frac{Lk}{m} a \sqrt{r^2 - a^2} - \frac{2Lk}{m} a y_{cm} \quad (10)$$

For the case where the surface deflection is less than the radius of the wheel, (10) becomes (11), where $a = \sqrt{r^2 - y_{cm}^2}$, from (6). For the case where this deflection is greater than the wheel radius, (10) becomes (12), where $a = r$.

$$\ddot{y}_{cm} = g - \frac{Lk}{m} r^2 \sin^{-1}\left(\frac{\sqrt{r^2 - y_{cm}^2}}{r}\right) - \frac{Lk}{m} y_{cm} \sqrt{r^2 - y_{cm}^2} \quad (11)$$

$$\ddot{y}_{cm} = g - \frac{Lk}{m} \frac{\pi}{2} r^2 - \frac{2Lk}{m} r y_{cm} \quad (12)$$

The horizontal (x_{cm}) motion of the robot depends on the traction force generated by the interaction between the wheel and the organ. The organs are generally coated with peritoneal fluid which is modeled as a viscous fluid as shown in Fig. 5, where the thickness of the fluid is exaggerated.

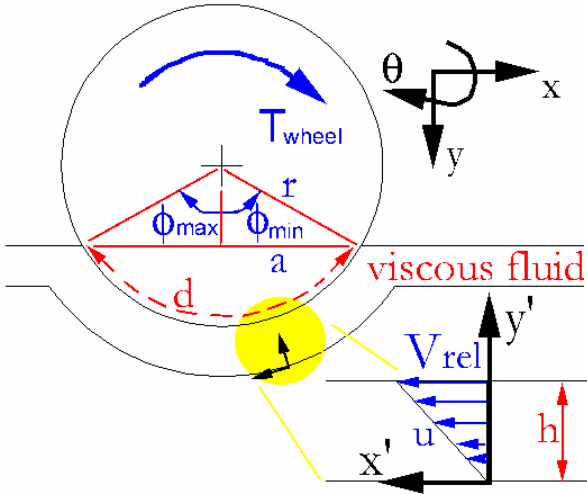


Figure 5. Peritoneal fluid model.

The shear stress at the wheel can be written as

$$\tau_{x'y'} = \mu \frac{\partial u}{\partial y'} = \mu \frac{V_{rel}}{h}, \quad (13)$$

where x' and y' are local axes, μ is the viscosity of the fluid, and u is the velocity profile of the fluid between the wheel and the organ. A linear profile is assumed, where V_{rel} is the relative velocity between the wheel surface and the organ, and h is the distance between the wheel and the organ. The distance h is assumed to be constant and is estimated as described in Section VI. V_{rel} is given by

$$V_{rel} = r\dot{\theta}_{cm} - \dot{x}_{cm} \cos\phi. \quad (14)$$

The total shear stress must be multiplied by the length of the wheel, L , and integrated over the contact length to give the total torque generated by the shear stress:

$$\begin{aligned} T_{shear} &= Lr^2 \int_{\phi_{min}}^{\phi_{max}} \tau_{x'y'} \partial\Omega \\ &= Lr^2 \int_{\phi_{min}}^{\phi_{max}} \frac{\mu}{h} (r\dot{\theta}_{cm} - \dot{x}_{cm} \cos(\Omega)) \partial\Omega, \quad (15) \\ &= \frac{2Lr^2\mu}{h} (\phi_{max} r\dot{\theta}_{cm} - \dot{x}_{cm} \sin(\phi_{max})) \end{aligned}$$

where Ω is a dummy variable and the integration limits are given by geometry and symmetry as

$$\phi_{min} = -\phi_{max} = -\sin^{-1}\left(\frac{a}{r}\right). \quad (16)$$

The shear stress can also be projected along the horizontal axis to estimate the horizontal force generated by the wheel/organ interaction, given by

$$\begin{aligned} F_{shear} &= \int_{\phi_{min}}^{\phi_{max}} r \cdot L \cdot (\tau_{x'y'} \cdot \cos\Omega) \partial\Omega \\ &= \frac{rL\mu}{h} \left[2r\dot{\theta}_{cm} \sin(\phi_{max}) - \dot{x}_{cm} \phi_{max} - \frac{\dot{x}_{cm}}{2} \sin(2\phi_{max}) \right], \quad (17) \end{aligned}$$

where the limits on Ω are given by geometry in Fig. 5.

Finally, the horizontal equation of motion can be written as follows,

$$F_{drawbar} = -m\ddot{x}_{cm} + F_{shear}. \quad (18)$$

The rotational equation becomes

$$J\ddot{\theta}_{cm} = T_{wheel} - T_{shear}, \quad (19)$$

where J is the rotational inertia of the robot and T_{wheel} is the input torque applied by the motor, to the wheel.

A Matlab™ application has been developed that incorporates the analytical model described above, defined by

(11), (18), and (19), to simulate wheel/tissue interaction. This simulation tool was verified with a series of experiments as described in Section VII.

V. EXPERIMENTAL SYSTEM

A laboratory system was created as shown schematically in Fig. 6a. This system consists of a linear slide that moves a wheel (Fig. 6b), similar in size, shape, and material to the proposed robot, across a model of an organ. The wheel is independently driven by a motor attached with a drive belt. The wheel assembly is mounted to a lever that is used to dictate the wheel/organ normal force. A load cell is used to measure the drawbar force, $F_{drawbar}$, and an inclinometer on the lever is used to determine surface deflections.

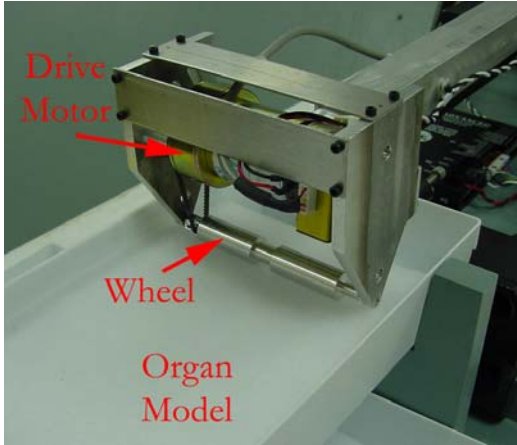
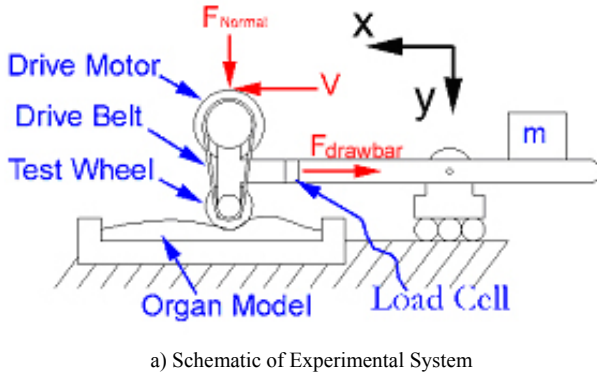


Figure 6. Experimental system.

VI. ORGAN MODELS AND PARAMETER IDENTIFICATION

Two different materials were used to replicate the characteristics of internal organs. The first organ model was a piece of foam because of the predictability and homogeneity of the mechanical properties. This model was used to confirm the simulation results from the analytical model presented above. The second organ model was a bovine liver used to emulate the *in vivo* operating conditions mobile robots will experience. Experiments were performed to identify the viscosity and stiffness characteristics for both models.

A. Viscosity

Experiments were performed to estimate the viscous coefficient (μ/h) in (13). During these experiments, the angular position of the wheel was held constant (no rotation) while the linear slide was used to translate the wheel horizontally across the surface of the each organ model. The drawbar forces and the contact lengths (ϕ_{max}) were determined during this motion from measurements of the load cell and inclinometer at each of five different linear velocities. When the rotational velocity is zero, the relative velocity between the wheel and the surface of the organ model equals the linear velocity of the slide (14). The drawbar force, $F_{drawbar}$, is also then equal to F_{shear} . A relationship between the known drawbar force and the known relative velocity can then be established using (17), allowing the ratio (μ/h) to be determined. This test was repeated three times for each of the five linear velocities at each of three normal forces for both organ models. A linear least-squares fit of the data to a friction model containing a combination of coulomb and viscous friction was then performed. Results for the bovine liver are shown in Fig. 7, where it is assumed that the frictional effects are symmetric for forward and reverse velocities.

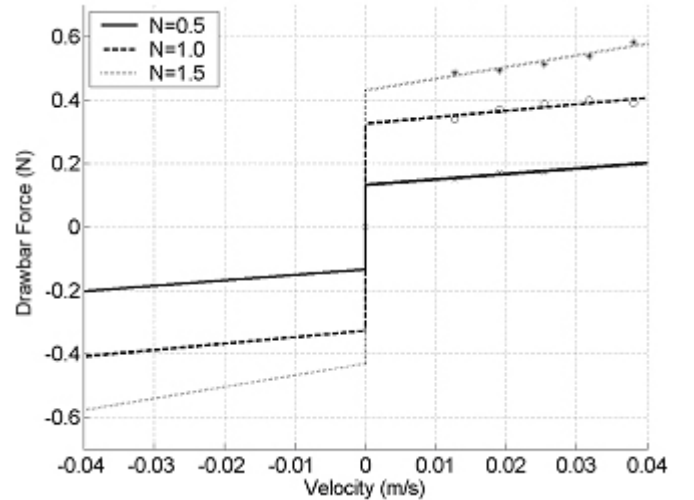


Figure 7. Least-Squares Fit for Determination of Viscous Effects.

B. Stiffness

Additional experiments were performed to estimate the stiffness coefficient, k , of both organ models. This was accomplished by placing a rigid plate of known area on each organ model and measuring the vertical deflection as various weights were placed on the rigid plate. Three separate sets of measurements were made for each organ model, with normal forces varying between 20 and 200 grams. The orientation of the plate was changed for each test to account for non-homogeneities in the surface material. The mass applied to the rigid plate was divided by the area of the plate to estimate the average applied pressure. Linear least-squares fits of the data were performed to determine the stiffness coefficient of each organ model, Fig. 8. The stiffness of the foam organ model was estimated to be 225,000 (N/m^2)/m, while the bovine liver stiffness was 415,000 (N/m^2)/m.

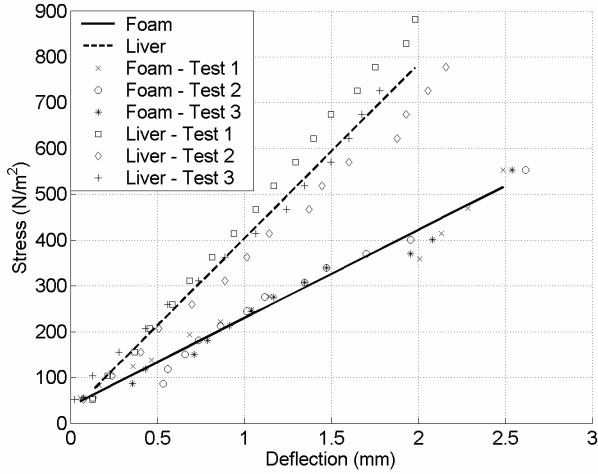


Figure 8. Stiffness Experiments for foam and bovine liver.

VII. COMPARISON OF EXPERIMENTAL AND SIMULATION RESULTS FOR A ROUND WHEEL

A. Experimental Procedure

A set of experiments was performed to first verify the analytical model described above, and then to determine the performance of several wheels on bovine liver.

In each experiment the wheel assembly was driven across the organ model at a fixed linear velocity of 2.54 cm/s while the angular velocity of the wheel was independently controlled at various slip ratios. The slip ratio is defined as

$$SR = \text{slip ratio} = \frac{\dot{x}_{cm}}{r\dot{\theta}_{cm}}, \quad (20)$$

where \dot{x}_{cm} is the linear forward velocity of the center of mass of the wheel, $\dot{\theta}_{cm}$ is the angular velocity of the wheel, and r is the wheel radius. The drawbar force was measured and averaged over a set of ten tests (e.g. Fig. 9). The total distance traveled was approximately 20 cm during each test. Experiments were performed at slip ratios of 0.5, 1, and 1.5, which represent positive slip (pull), no slip, and negative slip (skidding), respectively.

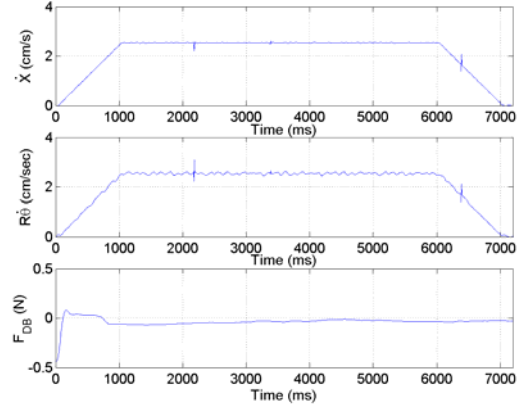


Figure 9. Time history of an example experiment.

B. Comparison Of Experimental And Simulation Results For A Round Wheel on the foam Organ Model

The analytical model was first used to determine the expected drawbar forces for a smooth aluminum wheel moving on the foam organ model, Fig. 10. Each line in the graph represents normal forces of 0.5, 1.0, or 1.5 times the weight, W , of the robot in Fig. 1 (28 grams). The experimentally determined values of viscosity and surface stiffness, as described in (6), were used in the simulations.

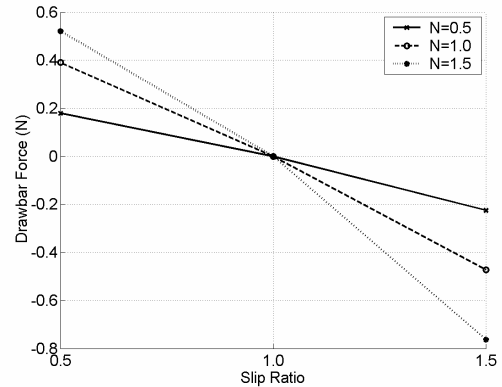


Figure 10. Simulated drawbar force for smooth wheel on foam organ model.

As shown in Figure 10, a larger normal force produces a larger drawbar force. When the slip ratio is 0.5, the wheel is pulling the linear slide and the drawbar force is positive. When the slip ratio is one, the wheel motion matches the motion of the slide and no drawbar force is generated. When the slip ratio is 1.5, the wheel is being pushed by the linear slide and the drawbar force is negative (i.e. skidding).

Figure 11 shows the experimental results obtained for motion of a smooth aluminum wheel on the foam organ model. Each point in the Figure represents the average drawbar force produced by the smooth aluminum wheel for ten independent experiments.

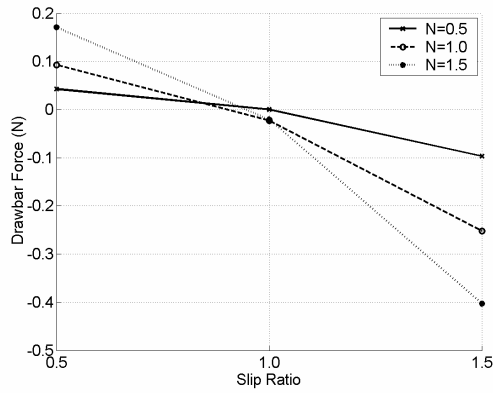


Figure 11. Experimental drawbar force for smooth wheel on foam organ model.

The simulation results predict a larger drawbar force by a factor of approximately three. However, both the simulation and experimental results have excellent agreement in terms of the relative wheel performance at both the various slip-ratios and the various normal forces (i.e. Fig. 11 is a scaled version of Fig. 10). The lower drawbar forces measured by the experimental system could result from energy dissipation in the organ model. The analytical model used in the simulation does not include damping in the organ (i.e. a purely elastic surface is assumed). The experimental system dissipates energy as the organ model is deformed as the wheel moves forward, and this decreases the drawbar force. In the simulation results, this energy is completely restored by the purely elastic organ model pushing on the back of the wheel. Future work will include a visco-elastic model.

These results do show that the analytical model predicts the correct trends for variations in normal forces and slip ratios.

VIII. EXPERIMENTAL COMPARISON OF THREE WHEEL DESIGNS

A. Three Wheel Designs

Further experiments were conducted to compare three different aluminum wheel geometries, as shown in Fig. 12. The first wheel is the smooth wheel described by the analytical model and discussed in the previous section. The second wheel (“female”) has eight small grooves, while the third (“male”) has larger grooves. The tests described above were repeated with each wheel on both the form and bovine liver organ models.

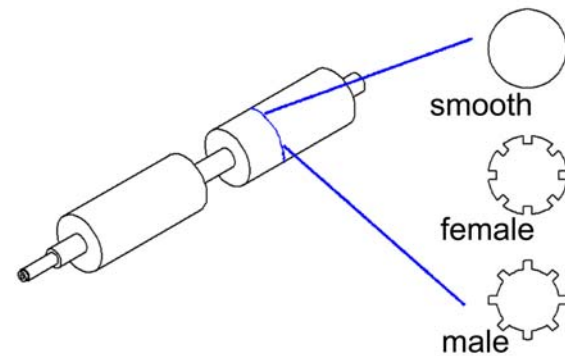


Figure 12. Different Wheel Designs; Smooth (top), Female (middle), and Male (bottom).

B. Smooth Wheel

1) Foam Organ Model

The experimental results for the smooth wheel on foam are shown in Fig. 11. The wheel produced a larger drawbar force with larger normal forces. Again, when the slip ratio is 0.5, the wheel is pulling the linear slide and the drawbar force is positive. When the slip ratio is 1.0, the wheel motion matches the motion of the slide and no drawbar force is generated. When the slip ratio is 1.5 the wheel is being pushed by the linear slide and the drawbar force is negative (i.e. skidding).

2) Bovine Liver Organ Model

The liver properties are similar to the expected *in vivo* conditions (the porcine liver is visible in Fig. 1). The liver is coated with peritoneal fluid that reduces the frictional coefficient (lower (μ/h)), leading to lower drawbar forces.

These test results are shown in Fig. 13. The drawbar forces generated by the smooth wheel are approximately a factor of two-three lower than the forces produced by the same wheel on foam. Furthermore, all the forces are negative, implying that the wheel produces very little traction and that the linear slide is always pushing the wheel across the surface of the liver. This is also suggested by the fact that the drawbar force is non-zero and negative even when the wheel motion matches the forward velocity (SR=1.0). These results suggest that a smooth wheel is not a good design for the robot wheels.

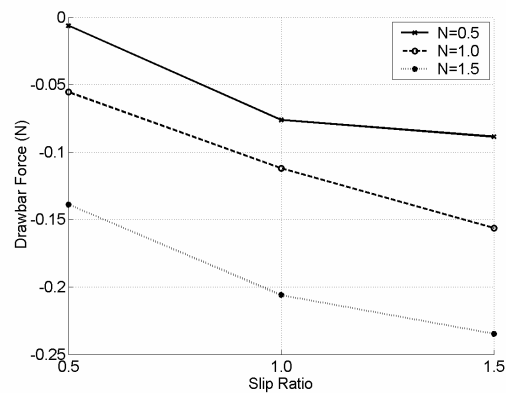


Figure 13. Experimental drawbar force for smooth wheel on bovine liver.

C. Female Wheel

1) Foam Organ Model

Fig. 14 shows the experimental results of a female wheel on foam. The trends and values for drawbar force are almost identical to those of the smooth wheel on foam (Fig. 11). This indicates that there is little difference in wheel performance.

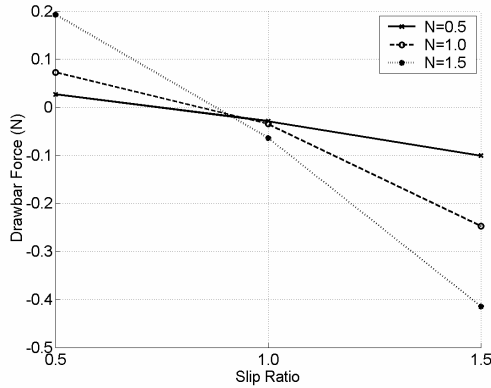


Figure 14. Experimental drawbar force for female wheel on foam .

2) Bovine Liver Organ Model

Fig. 15 shows experimental drawbar force measurements for the female wheel on liver. The trends are again similar to the smooth wheel on liver (Fig. 13) except that the wheel is capable of producing a positive drawbar force for a slip ratio of 0.5. This implies that the female wheel might be capable of moving. However, the drawbar force produced under a normal force corresponding to the weight of the robot is only 0.05 N, compared to the 0.27 N weight of the robot. It is not likely that this robot would be capable of climbing or moving up a hill.

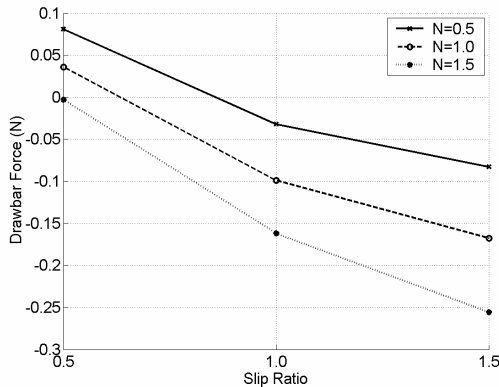


Figure 15. Experimental drawbar force for female wheel on bovine liver.

D. Male Wheel

1) Foam Organ Model

Fig. 16 shows the performance of the male wheel on foam. On foam, this wheel produces similar drawbar forces as compared to both the smooth wheel and female wheel.

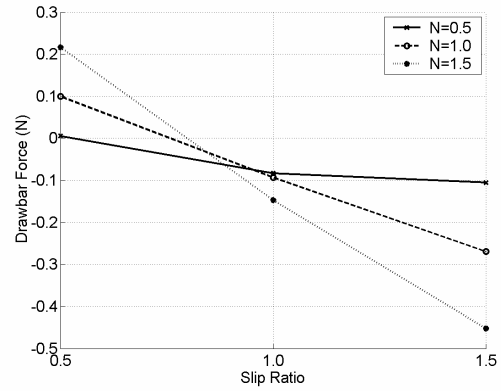


Figure 16. Experimental drawbar force for male wheel on foam organ model.

2) Bovine Liver Organ Model

Fig. 17 shows experimental drawbar force measurements for the male wheel on bovine liver. This wheel performs differently compared to the female wheel. First, the drawbar force corresponding to the weight of the robot ($N=1.0$) and a slip ratio = 0.5 is approximately 0.1 N, twice as much as the female wheel. Also, at a slip ratio of 0.5, each drawbar force is the same at each normal force. This suggests that the drawbar force for this case does not vary with normal force. It is possible that it is limited by the peritoneal fluid.

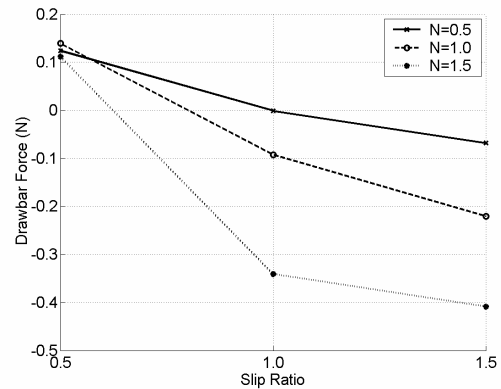


Figure 17. Experimental drawbar force for male wheel on bovine liver.

E. Conclusions on Wheel Designs

According to these experiments, the male wheel shows the best performance. On foam there is no significant difference between the different wheel designs. However, on the surface of the liver, the male wheel produces the highest drawbar force by a factor of two.

IX. CONCLUSIONS AND FUTURE WORK

This paper presents an experimental and theoretical analysis of *in vivo* wheeled mobility. An analytical model is presented that represents the compliance of internal organs. This model also represents the peritoneal fluid found in this environment. Model parameters were determined experimentally. Simulations of the drawbar force for various slip ratios and normal forces were compared. The simulation results produced

identical trends as compared to the experimental results. These results differed by approximately a factor of three and this discrepancy may result from the purely elastic model of the surface. Experimental results are also shown for three wheel designs operating on both a foam and bovine liver model of the *in vivo* environment.

Future work will include further development of the model including a visco-elastic surface and exploration of different wheel materials.

REFERENCES

- [1] Schippers, E., and Schumpelick, V., "Requirements and possibilities of computer-assisted endoscope surgery," *Computer Integrated Surgery: Technology and Clinical Applications*, 1996
- [2] Treat, M., "A surgeon's perspective on the difficulties of laparoscopic surgery," *Computer Integrated Surgery*, 1996.
- [3] Tendick, F., Jennings, R., Tharp, G., and Stark, L., "Perception and manipulation problems in endoscope surgery," *Computer Integrated Surgery: Technology and Clinical Applications*, 1996.
- [4] Wolfe, B., Gardiner, B., and Leary, B., et al: "Endoscopic cholecystectomy: analysis of complications," *Arch Surg* vol. 126, 1991.
- [5] Southern Surgeons Club, "A prospective analysis of 1518 laparoscopic cholecystectomies," *N.E. J. of Medicine*, vol. 324, pp 1073-1078, 1991.
- [6] Medtech Insight, Mission Viejo, CA, 2000.
- [7] Lo, P., et. al., "Which laparoscopic operations are the fastest growing in residency programs?," *Surgical Endoscopy*, vol 15., pp. S145, 2001.
- [8] Satava, R.M., "Surgical robotics: the early chronicles," *Surgical Laparoscopy, Endos. & Percutaneous Techniques*, vol. 12, no. 1, 2002.
- [9] Ballantyne, G.H., "Robotic surgery, telerobotic surgery, telepresence, and telementoring," *Surgical Endoscopy*, vol 16, pp. 1389-1402, 2002.
- [10] Schurr, M.O., Buess, G., Neisius, B., and Voges, U., "Robotics and telemanipulation technologies for endoscopic surgery," *Surgical Endoscopy*, vol. 14, pp. 375-381, 2000.
- [11] Sackier, J. and Wang, Y., "Robotically enhanced surgery: from concept to development," *Surgical Endoscopy*, vol 8, pp. 63-66, 1994.
- [12] Kim, V.B., Chapman, W.H.H., Albrecht, R.J., Bailey, B.M., Young, J.A., Nifong, L.W., and Chitwood, W.R., "Early experience with telemanipulative robot-assisted laparoscopic cholecystectomy using da vinci," *Surgical Laparoscopy, Endoscopy & Percutaneous Techniques*, vol. 12, no. 1, pp. 33-44, 2002.
- [13] Kang, H. and Wen, J.T., "Robotic assistants aid surgeons during minimally invasive procedures," *IEEE Engineering in Medicine and Biology*, pp. 94-104, Jan/Feb, 2001.
- [14] Rentschler, M., Hadzialic, A., Dumpert, J., Platt, S., Farritor, S., Oleynikov, D., "In Vivo Robots for Laparoscopic Surgery." *Proceedings of the 2004 Medicine Meets Virtual Reality Conference (MMVR 12)*, Newport Beach, CA, January 2004.
- [15] M. G. Bekker, "Off the Road Locomotion", U. of Michigan Press, 1960.
- [16] O. Onafeko and A.R.. Reece, "Soil Stresses and Deformations Beneath Rigid Wheel", *J. of Terramechanics*, Vol. 4, No.1, pp. 59 to 80, 1967.
- [17] Wong and Reece 1967.
- [18] Iagnemma, K., Shibly, H., and Dubowsky, S., "On-line terrain Parameter estimation for planetary rovers." *IEEE International Conference on Robotics and Automation (ICRA 02)*, Washington, DC, May 2002.
- [19] Selvadurai, A.P.S., "Elastic Analysis of Soil-Foundation Interaction" Elsevier Scientific Publishing Company, 1979.
- [20] Jo-Yung Wong and A.R.. Reece, "Prediction of Rigid Wheel Performance Based on the Analysis of Soil-Wheel Stresses, Part I. Performance of Driven Rigid Wheels", *J. of Terramechanics*, Vol. 4, No.1, pp. 81 to 98, 1967.